ACS Sustainable Chemistry & Engineering

pubs.acs.org/journal/ascecg

Research Article

Enhancing Resource Circularity in Aluminum Production through Nanofiltration of Waste Cryolite

Trent R. Lee, Zi Hao Foo, Vinn Nguyen, and John H. Lienhard*

Cite This: ACS Sustainable Chem. Eng. 2025, 13, 846−858

Read Online

ACCESS | Metrics & More | Article Recommendations | Supporting Information

ABSTRACT: This study presents a novel approach to the selective separation of aluminum from waste cryolite electrolyte with two nanofiltration membranes: a conventional polyamide membrane and a membrane coated with a polyelectrolyte layer. Utilizing transmission electron microscopy and Fourier transform infrared spectroscopy, we find that the polyelectrolyte coating significantly increases the density of positively charged ammonium groups on the membrane surface, thereby enhancing the Donnan exclusion of aluminum ions. Notably, the polyelectrolyte coating enhances the sodium/aluminum separation factor by 55%. Our experimental results demonstrate that the coated membrane sustains high aluminum rejection rates, averaging 99.1%, while permitting substantial permeation of sodium, lithium, and potassium ions. This selective permeability is pronounced at lower pH levels, where the sodium/aluminum separation factor peaks at 102.02 for chloride-rich waste cryolite. Our process modeling using the Donnan steric pore model with dielectric exclusion substantiates the practical viability of Donnan-enhanced nanofiltration for processing waste cryolite. Our module-scale analysis indicates that the efficient aluminum concentration in the retentate, achieving a sodium/aluminum ratio of approximately 2.6, is viable for upcycling cryolite electrolyte and promoting a circular aluminum economy. Furthermore, the aluminum-depleted permeate, with aluminum cationic composition as low as 0.00194%, makes ample progress toward a benignly disposable effluent, reducing the aluminum industry's environmental footprint.

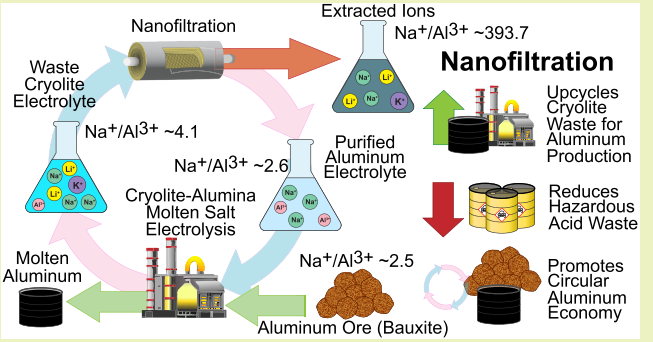

KEYWORDS: *Aluminum, Circular Economy, Nanofiltration, Upcycling, Waste Cryolite.*

1. INTRODUCTION

Aluminum is the second most sought-after metal after steel, and its versatile applications in automotive, aerospace, and construction sectors have driven growing demand and production.[1,2] However, this increase in production also amplifies environmental challenges, especially from waste generated during ore processing.[3−5]

The first step in aluminum production, bauxite mining, is a large-scale operation involving extensive land excavation, which leads to topsoil erosion, reduced biodiversity, and decreased agricultural productivity.[6,7] Waste from bauxite mining and processing contaminates water, soil, and wildlife with heavy metals, iron oxide, and aluminum hydroxide.[8] The mined bauxite is crushed and refined through the Bayer process, which uses sodium hydroxide (NaOH) to extract alumina (Al_2O_3), producing an alkaline waste called red mud.[9] Red mud, containing toxic metals like arsenic, chromium, and nickel, along with NaOH, sodium carbonate (Na_2CO_3), and sodium aluminates ($NaAlO_2$), has a high pH, and it causes significant health and environmental problems, especially in aquatic ecosystems.[8,10−12] Storage of red mud near water bodies can lead to heavy metal leaching, and contact with red mud may have immediate health effects like skin burns and respiratory irritation.[11,13] Annually, about 120 million tons of red mud are generated globally (4−5 tons per ton of aluminum) and this figure is expected to rise with increasing aluminum production.[14,15]

After the Bayer process, alumina undergoes cryolite-alumina molten salt electrolysis, known as the Hall−Héroult process, which is the primary method of aluminum production.[16] In this process, a cryolite (Na_3AlF_6) electrolyte is essential for dissolving Al_2O_3. Over time, as aluminum is depleted from the electrolyte, the Na/Al ratio increases; however, an Na/Al molar composition ratio (CR) held around 2.5 is necessary for efficient production.[17,18] When the electrolyte becomes too impure with Na, Li, and K, it must be replaced with cleaner cryolite and the spent electrolyte becomes a waste product.

Received: September 1, 2024
Revised: December 19, 2024
Accepted: December 20, 2024
Published: January 6, 2025

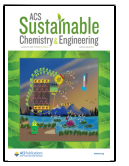

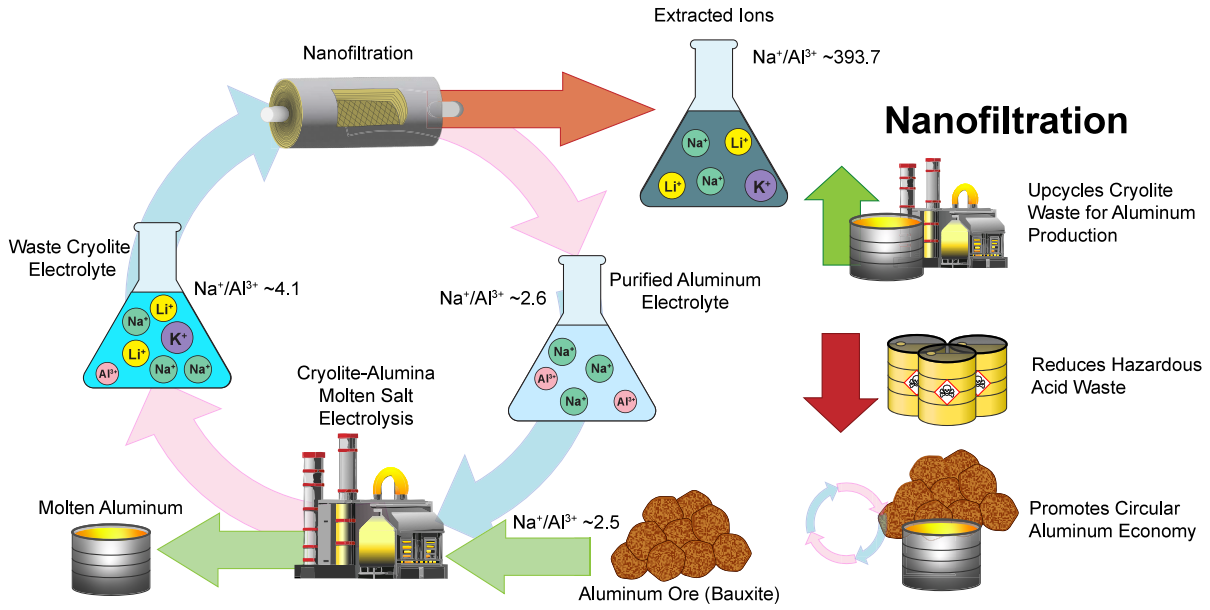

Figure 1. Schematic representation of the role of nanofiltration (NF) in purifying waste cryolite. Waste cryolite from molten salt electrolysis consists of Al^{3+} ions and impurities, mainly Na^+ and smaller quantities of K^+, Li^+, and Ca^{2+}. NF selectively rejects the passage of Al^{3+}, concentrating on other impurities into the permeate stream. The result is a purified aluminum electrolyte stream that can be upcycled back into the cryolite–alumina molten salt electrolysis process.

Table 1. Ionic composition of an industrial aluminum waste cryolite solution, as reported by Tang et al.[18]

Solution Type	Na^+	K^+	Li^+	Ca^{2+}	Al^{3+}	Cl^-	SO_4^{2-}	TDS
Sulfate-Rich Cryolite	15.46	1.78	1.94	0.07	4.41	0	70.60	94.66
Chloride-Rich Cryolite	15.46	1.78	1.94	0.07	4.41	52.11	0	76.17

Waste management and recycling of aluminum cryolite electrolyte are currently under-researched. Existing studies mainly focus on spent pot lining and spent carbon anodes.[19] Traditional disposal methods for spent electrolyte, such as cooling and landfilling, result in soil and groundwater contamination with harmful substances like fluoride (F) and aluminum (Al), causing significant ecological damage.[18,20] Reusing cryolite waste with new electrolyte to reduce costs complicates the Hall-Héroult process due to introduced impurities that require further purification.[21] An aluminum plant producing 200,000 tons annually generates approximately 2,800 tons of waste electrolyte.[21] Yet, aluminum cryolite electrolyte waste remains critically underexplored, posing a significant challenge to the growing aluminum industry.

Addressing the environmental impacts of both bauxite mining and aluminum cryolite electrolyte waste is vital to the sustainable management of aluminum production. A potential strategy to address these challenges is recycling aluminum waste, which offers a dual benefit: the simultaneous treatment of cryolite waste and the reduction of the need for newly mined bauxite. Recycling aluminum from waste cryolite can not only detoxify the waste but also recover valuable elements, providing a promising circular economy for aluminum production.

A few proposed methods for recycling aluminum cryolite have shown promise. Wu et al. introduced a multistage process involving Al^{3+} leaching and fluoride recovery to extract valuable components like lithium, sodium, potassium, calcium, and fluoride.[22] Tang et al. developed a "sulfated roasting-calcine water leaching-aluminum precipitation" method to recover lithium fluoride and aluminum sulfate.[18] Building on these researchers' work, we explore membrane systems for efficient recycling. Particularly, we examine nanofiltration (NF) given its recent promise in resource recovery.[23−25] A traditional NF membrane, consisting of an active polyamide layer on polysulfone supports, is compared to a "coated" variant with an additional polyelectrolyte. The coating is hypothesized to enhance cation selectivity as a result of Donnan exclusion.[23] Our goal is to separate Al^{3+} from other ions in the waste cryolite electrolyte, allowing monovalent ions like Na^+, K^+, and Li^+ to permeate while retaining Al^{3+}. We develop a process using an NF spiral-wound module to upcycle waste cryolite, generating a permeate with minimal Al for potentially cleaner disposal and an Al-rich retentate meeting cryolite ratio requirements for alumina molten salt electrolysis, thereby promoting resource circularity in aluminum production.

We build on Tang et al.'s process after the sulfated roasting and water-leaching steps, focusing on a representative solution comprising mainly Na, Al, Li, K, and Ca. As illustrated in Figure 1, we then run two variants of this solution—one sulfate-rich and the other chloride-rich—through an NF membrane setup, targeting Na/Al separation, since the K, Li, and Ca percentages by weight are relatively low, as shown in Table 1.[18] To facilitate the recycling of aluminum dissolved in the waste cryolite, we aim to produce Na-rich permeate streams through nanofiltration while retaining the dissolved

https://doi.org/10.1021/acssuschemeng.4c07268
ACS Sustainable Chem. Eng. 2025, 13, 846−858

aluminum in the retentate stream.[18] The retained aluminum electrolyte can then be reblended with alumina, which is processed from bauxite ore. Based on recent analysis, to enable aluminum recycling from waste cryolite solutions, the Na/Al concentration ratio of the retentate stream must be held to ~2.5.[18] Therefore, nanofiltration conditions with high Na−Al separation are crucial for optimizing this process. We conduct coupon-scale experiments to evaluate NF's effectiveness in treating aluminum waste cryolite. We first characterize both uncoated and coated NF membranes for upcycling aluminum in a waste cryolite treatment. After identifying the coated membrane's superior Na/Al separation performance, we conduct experiments under various pHs, solution compositions, and water flux parameters using a coated membrane coupon. We also perform aging tests to assess the coated membrane's durability with acidic waste cryolite. Overall, we collected 200 ion rejection measurements, which we used to calibrate a transport model. Finally, we apply this model to a commercial coated spiral-wound NF membrane for module-scale computational analysis in terms of specific energy cost and permeate aluminum composition as a function of the waste volume reduction.

2. METHODS

2.1. Experimental Section. *2.1.1. Chemicals and Materials.* Building upon our prior collaborative work with Nitto-Denko, we acquire the same two variants of semiaromatic nanofiltration (NF) membranes from Nitto-Denko (Osaka, Japan).[23] The first membrane consists of a conventional polyamide active layer (30−40 nm) that is polymerized on a polysulfone support and woven into a polyester mesh (100−150 μm).[23] The polyamide layer has an isoelectric point at a pH of ~5.5 and is the product of a conventional interfacial polymerization between piperazine and trimesoyl chloride.[26,27] The second membrane has a highly cross-linked and acid-resistant polyelectrolyte coating (35−50 nm) that is condensed onto the polyamide layer;[23] the resulting active bilayer of the composite NF membrane possesses a positive ζ potential across the pH spectrum, as delineated in our prior publication.[23] The NF membranes are stored in buffered solutions containing 3 wt % NaCl and soaked in deionized water for 24 h before use.

We conducted bench-scale experiments with synthetic waste cryolite solutions that are a product of acid leaching in H_2SO_4 and HCl, to characterize the ion selectivity performance of the two NF membranes.[18] We based our model solution compositions on the industrially relevant data reported in Tang et al.,[18] ensuring that both the ionic composition and pH levels reflect real-world cryolite waste characteristics, rather than theoretical approximations. This method anchors our experimental conditions firmly in practical, industry-derived values. The sulfate- and chloride-rich solutions are utilized to analyze the impact of anion composition from acid leaching in H_2SO_4 and HCl, respectively. Anhydrous sulfates and chlorides of Na^+, K^+, Li^+, Ca^{2+}, and Al^{3+}, in addition to H_2SO_4 (51%), HCl (37%), and NaOH (>98%), are acquired from MilliporeSigma. We use Type I ultrapure water (18.2 MΩ cm) to prepare the feed solutions for the membrane filtration experiments. The elemental compositions of the synthetic cryolite solutions are tabulated in Table 1. The feed and permeate channel spacers are obtained from a commercial spiral wound module. A full account of the experimental apparatus can be found in Section 1.1 of the Supporting Information (SI).

2.1.2. Membrane Characterization. To complement coupon-scale filtration experiments, we characterize the structure and functional group density in the membrane's active layer, leveraging the measurements reported in our prior publication.[23] The water permeability coefficient for the uncoated polyamide membrane was measured to be approximately 9 LMH bar^{-1}, which decreases by up to 18.7% upon the addition of the polyelectrolyte coating. We employ transmission electron microscopy (TEM, Philips CM 100) to visualize the polyelectrolyte and polyamide active layers within the coated NF membrane and use Fourier transform infrared spectroscopy (FTIR, Nicolet iS50 FTIR Spectrometer) to identify the functional groups within the active layer(s).

To characterize the membranes' selectivity and permeability, we employ a bench-scale plate-and-frame apparatus.[28] To test the membranes' durability and lifespan performance, we aged the membranes in 0.5 M HCl for up to 4 weeks and assessed the selectivity integrity with periodic ion rejection experiments. In total, we collected 200 rejection measurements from 40 unique permeate experimental samples with the bench-scale setup using both the uncoated and coated membranes. The samples represent various operating conditions, including solution pH ranging from 1 to 3, and measured feed pressures ranging from 34 to 46 bar, across the two distinct cryolite compositions.[28] The compiled experimental data are detailed in SI.

We perform the experiments at a temperature of 20 ± 0.5 °C with a cross-membrane flow velocity of 0.17 m s^{-1}. For each experiment, we initially pressurize the membrane coupon at 34 bar for 1 h and then equilibrate it to the feed solution for 15 min before taking the initial samples from the feed and permeate solutions. During the course of the experiments, the ion concentration and volume in the feed reservoir, approximately 4 L, remained effectively constant given the relatively small amount of permeate removed. Consequently, we did not observe any significant changes in concentration within the feed solution, minimizing potential impacts on flux over time. We collect samples in chilled centrifuge tubes before analyzing the ionic compositions with inductively coupled plasma optical emission spectroscopy (Agilent ICP-OES 5100), using standards from MilliporeSigma (TraceCERT). Based on triplicate sampling, the maximum uncertainty in concentration measurements is below 4.3%.

In this study, we standardized pressure rather than flux to correlate directly with energy expenditure for pumping, a critical factor for industrial scaling.[29] Flux standardization is challenging due to significant variations in the inherent permeability of the uncoated and coated membranes across different solution conditions (e.g., pH, composition, salinity).[30] The coated membrane exhibits lower flux due to increased hydraulic resistance for water transport. Nevertheless, despite the doubling of the membrane's active layer thickness with the polyelectrolyte coating, its water permeability decreased less than proportionally (by approximately 20%) due to the higher porosity of polyelectrolytes compared to polyamides.[23] This allows the coated membrane to retain sufficient permeability for the aluminum cryolite treatment.

We measure and calculate the permeate water flux with eq 1.[31] Based on experiments with ultrapure water, we calculate the water permeability coefficients with eq 2.[32]

$$J_w = \frac{\Delta m}{\rho_w A_m \Delta t} \tag{1}$$

$$A_w = \frac{J_w}{\Delta P} \tag{2}$$

In the first equation, J_w [L m^{-2} h^{-1}] is the permeate water flux, while Δm [kg], ρ_w [kg L^{-1}], A_m [m^2], and Δt [s] are the change in permeate mass, solution density, membrane cross-sectional area, and time, respectively. In the second equation, A_w [L m^{-2} h^{-1} bar^{-1}] is the water permeability coefficient and ΔP [bar] corresponds to the transmembrane pressure. We calculate the rejection of the different ion species with eq 3, utilizing the ion concentrations from ICP.[33] We compute the separation factor ($SF_{i/j}$) between species i and j with eq 4.

$$R_i = 1 - \frac{C_{i,p}}{C_{i,f}} \tag{3}$$

$$SF_{Na/Al} = \frac{C_{Na,p}/C_{Al,p}}{C_{Na,f}/C_{Al,f}} \tag{4}$$

https://doi.org/10.1021/acssuschemeng.4c07268
ACS Sustainable Chem. Eng. 2025, 13, 846−858

Equation 3 and eq 4 determine the species' rejection (R_i) and separation factor ($SF_{Na/Al}$), where $C_{i,f}$ [mol L^{-1}] and $C_{i,p}$ [mol L^{-1}] are the concentrations of species i in the respective feed (f) and permeate (p) solutions. Here, the separation factor is defined as the change in the concentration ratio between species i and species j, between the permeate and feed solutions.[33]

Given the variability in cryolite waste composition across aluminum refineries, we selected a solution composition based on the hypersaline inorganic profile reported in Tang et al.,[18] representative of typical cryolite waste. This choice allows us to evaluate the membrane performance under realistic, high-salinity conditions. Further, a combination of chloride and sulfate-based strong acids (e.g., HCl and H_2SO_4) is used in processing, resulting in a waste stream that may contain chloride, sulfate, or a mixture of both anions. To account for this variability, we tested both pure chloride and pure sulfate cryolite solutions in this study. This approach allows us to define the left and right bounds of performance, with expected results for mixed chloride−sulfate solutions likely falling between these two extremes.

2.2. Analysis. *2.2.1. Computational Framework.* We calibrate the Donnan-steric pore model with dielectric exclusion (DSPM-DE) using the ion rejection measurements to facilitate module-scale analysis.[26] The extended Nernst−Planck equation describes species transport in the DSPM-DE model (eq 5), accounting for diffusion driven by concentration gradients, bulk solution transport by convection, and electromigration by Coulombic forces.[34]

$$N_i = K_{i,a} c_i J_w - K_{i,d} D_{i,\infty} \nabla c_i - K_{i,d} D_{i,\infty} \frac{z_i c_i F}{RT} \nabla \Psi \tag{5}$$

In eq 5, N_i [mol m^{-2} h^{-1}] denotes the flux of the solute. $K_{i,a}$ and $K_{i,d}$ are the convection and diffusion hindrance coefficients, $D_{i,\infty}$ [m^2 s^{-1}] is the bulk diffusion coefficient, c_i [mol L^{-1}] is the molar concentration, z_i is the species' valency, and T [K] and Ψ [V] are the temperature and electric potential, respectively. F [C mol^{-1}] and R [J mol^{-1} K^{-1}] are the Faraday and ideal gas constants, respectively.

In this model, we assume the membrane's structure is rigid with tortuous channels and a constant surface diameter.[26] We use hindered transport theory to determine the convection and diffusion hindrance coefficients,[35] as provided by eq 6 for convection and eqs 7 and 8 for diffusion, respectively.

$$K_{i,a} = \frac{1 + 3.867\lambda_i - 1.907\lambda_i^2 - 0.834\lambda_i^3}{1 + 1.867\lambda_i - 0.741\lambda_i^2} \tag{6}$$

$$K_{i,d} = (1 + \frac{9}{8}\lambda_i \ln(\lambda_i) - 1.56\lambda_i + 0.53\lambda_i^2 + 1.95\lambda_i^3 - 2.82\lambda_i^4 + 0.27\lambda_i^5 + 1.10\lambda_i^6 - 0.44\lambda_i^7)/(1 - \lambda_i)^2 \tag{7}$$

for $\lambda_i \in [0, 0.95]$, and

$$K_{i,d} = 0.984\left(\frac{1 - \lambda_i}{\lambda_i}\right)^{5/2} \tag{8}$$

for $\lambda_i \in (0.95, 1]$. Here, λ_i represents the ratio of a species i's Stokes radius to the membrane's pore radius.

To resolve the boundary conditions, we utilize the electroneutrality constraints in the bulk solution and within the NF membrane's nanopores, as expressed by eqs 9 and 10:

$$\sum_i^N z_i c_{i,\text{bulk}} = 0 \tag{9}$$

$$\chi_d + \sum_i^N z_i c_{i,\text{mem}} = 0 \tag{10}$$

Here, $c_{i,\text{bulk}}$ [mol L^{-1}] and $c_{i,\text{mem}}$ [mol L^{-1}] are the concentrations of species i in the bulk and inside the nanopores, respectively, and χ_d [mol L^{-1}] is the active layer's volumetric charge density.[35] We assume that the fluxes of different neutral species are independent.[36] In contrast, the transport of charged species is coupled because of the electric potential gradient created within the active layer to maintain electroneutrality.[28]

For boundary conditions, we apply isoactivity conditions along the solution−membrane interface, as seen in eq 11, to ensure the continuity of Gibbs free energy across the interface:[37]

$$\frac{(\gamma_i c_i)_{\text{mem}}}{(\gamma_i c_i)_{\text{bulk}}} = \Phi_{i,\text{st}} \Phi_{i,\text{do}} \Phi_{i,\text{di}} \tag{11}$$

Here, $\Phi_{i,st}$, $\Phi_{i,do}$, and $\Phi_{i,di}$ represent the steric, Donnan, and dielectric exclusion partition coefficients, respectively. These coefficients quantify the effects that influence a solute's partitioning behavior between the membrane pore environment and the bulk solution.[26] The net partition coefficient of a solute is determined by the ratio of the solute's activity within the membrane's pores to its activity in the bulk solution, encapsulating the combined impacts of steric, Donnan, and dielectric exclusion mechanisms.[35] Steric exclusion is the process by which solutes are filtered based on size by the membrane's pores.[38] Donnan exclusion results from electrostatic potentials at the solution−membrane interface, which impedes ions of the same charge as the membrane from entering its pores.[39] Dielectric exclusion occurs when ions encounter an energy barrier posed by the membrane pores' dielectric properties, leading to their repulsion.[40]

For steric exclusion, the ability of solutes to enter the membrane pores is strictly governed by their size relative to the pore radius of the membrane.[26] Solutes that exceed the membrane's pore radius are effectively precluded from entering, as their dimensions are too large to pass through the pore openings.[26] Conversely, solutes that are smaller than the pore radius have a size-dependent probability of entry, which is quantified by eq 12 and eq 13.[26,41]

$$\Phi_{i,\text{st}} = (1 - \lambda_i)^2, \quad \text{for } \lambda_i \in [0, 1] \tag{12}$$

$$\Phi_{i,\text{st}} = 0, \quad \text{otherwise} \tag{13}$$

Here, λ_i is the ratio of the solute Stokes radius to the expected membrane pore radius.

In Donnan exclusion, the Donnan potential ($\Delta\Psi_D$ [V]), originating from ion concentration discontinuities at the solution−membrane interface, dictates the Donnan exclusion partition coefficient, as outlined in eq 14.[39] This potential influences ion transport, favoring the entry of counterions (oppositely charged relative to the membrane's active layer) into the pores, while deterring co-ions (similarly charged) from penetration.[42]

$$\Phi_{i,\text{do}} = \exp\left(-\frac{z_i F}{RT} \Delta\Psi_D\right) \tag{14}$$

The dielectric exclusion phenomenon arises from the energy barrier created by the restricted mobility and confinement of water molecules within the nanoscale pores of the membrane.[40,43,44] This energy barrier impacts the transport of ions through the membrane, and is commonly estimated based on differences in solvation energies.[34] The dielectric exclusion coefficient is quantified in eq 15, employing the Born model's initial approximation for solvation energies to help elucidate the process.[45]

$$\Phi_{i,\text{di}} = \exp\left[-\frac{z_i^2 e^2}{8\pi k_B T \varepsilon_0 r_i}\left(\frac{1}{\varepsilon_{\text{mem}}} - \frac{1}{\varepsilon_{\text{bulk}}}\right)\right] \tag{15}$$

Here, ε_{mem} and ε_{bulk} are the relative permittivities in the membrane's pore and bulk solution.

Further, concentration boundary layers form along the solution−membrane interface during filtration.[35] We represent the ion concentrations along this boundary with concentration polarization effects from Geraldes and Alves.[41] We use eq 16, which gives the total ion flux within the concentration boundary layers as the sum of the diffusive, convective, and electromigrative fluxes.[41]

$$N_i = \overline{k}_{i,c}(c_{i,\text{int}} - c_{i,b}) + J_w c_{i,\text{int}} - z_i c_{i,\text{int}} D_{i,\infty} \zeta_{\text{int}} \frac{F}{RT} \tag{16}$$

https://doi.org/10.1021/acssuschemeng.4c07268
ACS Sustainable Chem. Eng. 2025, 13, 846−858

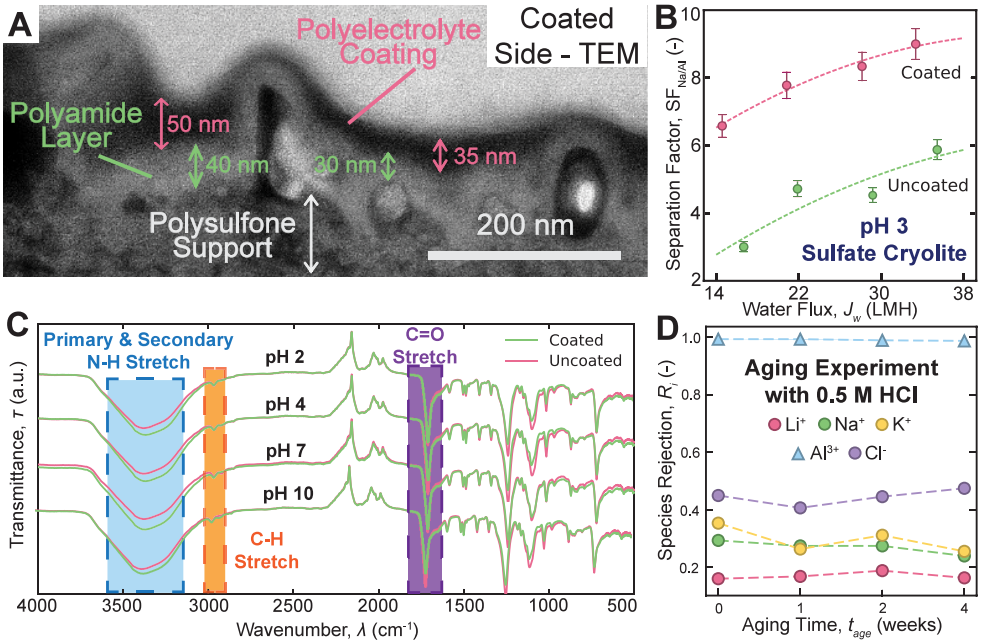

Figure 2. (A) Transmission electron microscopy analysis of the coated NF membrane's cross-section. Adapted with permission from our prior publication, ref 23. Copyright 2024 Wiley. (B) Plot of the Na/Al separation factor for both the uncoated and coated NF membranes as a function of transmembrane flux, based on coupon-scale experiments with pH 3 sulfate-rich cryolite solutions. (C) Fourier transform infrared (FTIR) spectroscopy of the coated membrane. Adapted with permission from our prior publication, ref 23. (D) Aging experiments are conducted to confirm the stability of the coated NF membrane upon exposure to acidic conditions for extended periods.

We calculate $k_{i,c}$, the mass transfer coefficient, from experimental empirical correlations for our bench-scale setup.[46]

$$k_{i,c} = 1.121 \times 10^{-4} \times \left(\frac{v_w}{0.239}\right)^{0.79} \tag{17}$$

Here, v_w [m s^{-1}] is the cross-flow velocity through the membrane.

Cumulatively, our ion transport model assumes the following:

1. The membrane's pores are tortuous cylindrical channels.
2. The charge density and pore radius are statistical averages and are uniformly distributed across the active layer.
3. The solutions within the membrane pores and in the bulk remain neutral.
4. Ions in the solutions remain completely ionized.
5. The solutes are depicted as ionic spheres with a hydration shell.
6. The solutes travel in one direction, orthogonal to the surface of the membrane.
7. The hindrance factor models can be used to describe the transport of ions through a porous membrane.
8. The transport of neutral solutes occurs independently, while the transport of charged solutes is coupled by the electrical potential.

2.2.2. Module-Scale Simulations. Our membrane allows a significant amount of monovalent ions, such as Na^+, K^+ and Li^+, to permeate through, a feature enabled by the Donnan exclusion mechanism. This selective monovalent ion permeation reduces the effective osmotic pressure difference across the membrane, even when the feed solution's osmotic pressure is high. By lowering the actual osmotic gradient, the membrane can operate effectively in hypersaline environments, addressing a key challenge associated with high-salinity waste treatment in membrane-based processes.

We regress the four hyperparameters of the DSPM-DE model independently from various subsets in the experimental data, with each subset equating to a process condition with a specific feed composition and pH. We employ a global optimization algorithm for the parametric regression, as delineated in our prior publication.[28] Then, we integrate the ion flux predictions from the DSPM-DE model with a forward Euler scheme to project resultant permeate concentrations of an industrial, spiral-wound NF module.[47] The spiral-wound module's dimensions are based on a commercial variant of the coated membrane (Nitto-Denko PRO-XS1), which has a length of 1.02 m and an effective area of 37.2 m^2. We use eq 18 to determine the permeate cation composition, by calculating the molar ratio of cation i to the total cation concentration.[48]

$$\chi_i = \frac{C_{i,p}}{\sum_j^{N_{cat}} C_{j,p}} \tag{18}$$

Here, χ_i is the permeate composition of cation i, N_{cat} is the number of dissolved cations, and j represents a specific cation (Na^+, K^+, Li^+, Ca^{2+}, and Al^{3+}).

Equation 19 derives the specific energy consumption relative to the molar quantity of aluminum extracted. This computation incorporates eq 20: the electrical work used for pumping the feed and the flow energy recovered through pressure exchangers. We assume the pump and pressure exchanger efficiencies are 0.75 and 0.8, respectively.[49]

$$SEC_{Al} = \frac{\dot{W}_{in}}{C_{Al,r}\dot{V}_r} \tag{19}$$

$$\dot{W}_{in} = \frac{\dot{V}_f \Delta P_{mem}}{\eta_{pump}} - (\dot{V}_f - \dot{V}_p)\Delta P_{mem}\eta_{px} \tag{20}$$

Here, SEC_{Al} [kWh mol^{-1}] is the specific electrical energy consumption and $\dot{W}_{in}$ [W] is the net electrical power consumed by the entire process. $\dot{V}$ [m^3 s^{-1}] is the volumetric flow rate, set at 0.001 m^3 s^{-1} for the feed stream, which is subscripted with f. ΔP_{mem} [Pa] is the difference in transmembrane pressure between the feed and the permeate streams. η is the efficiency for the pump and pressure exchanger, subscripted by pump and px accordingly.

As described by eq 21, waste volume reduction (WVR) is defined as the ratio of the permeate volumetric flow rate to that of the feed stream, accounting for the production of Na- and K-rich streams that can potentially be disposed of in an environmentally benign manner. Following spiral-wound NF treatment, we calculate the concentration

https://doi.org/10.1021/acssuschemeng.4c07268
ACS Sustainable Chem. Eng. 2025, 13, 846−858

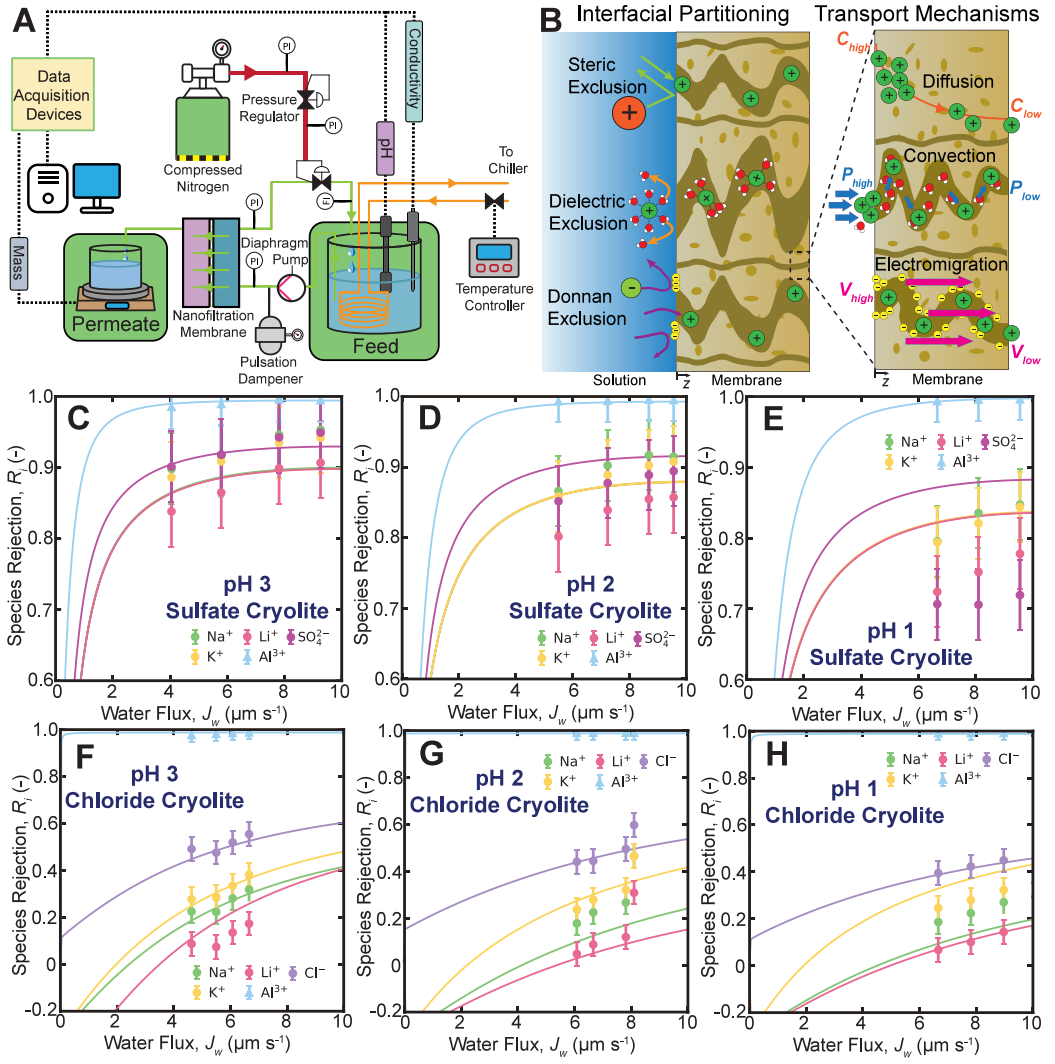

Figure 3. (A) Schematic diagram illustrating the experimental apparatus for coupon-scale membrane characterization. (B) Visualization of the partitioning and mobility selectivity mechanisms in nanofiltration.[26] Plots of the species rejection of the sulfate-rich waste cryolite solutions as a function of transmembrane flux in the case of (C) pH 3, (D) pH 2, and (E) pH 1. Likewise, the species rejections from the experiments with chloride-rich waste cryolite solutions are plotted for (F) pH 3, (G) pH 2, and (H) pH 1.

of Na and Al ions in the retentate stream to determine the product Na/Al composition ratio ($CR_{Na/Al}$) using eqs 22 and 23.[18] The derivation of eq 22 is detailed in Section S2 of the Supporting Information.

$$\mathrm{WVR} = \frac{\dot{V}_\mathrm{p}}{\dot{V}_\mathrm{f}} \tag{21}$$

$$C_{i,\mathrm{r}} = \frac{C_{i,\mathrm{f}}\cdot(1 - \mathrm{WVR} + \mathrm{WVR}\cdot R_i)}{1 - \mathrm{WVR}} \tag{22}$$

$$\mathrm{CR}_{\mathrm{Na/Al}} = \frac{C_\mathrm{Na}}{C_\mathrm{Al}} \tag{23}$$

3. RESULTS AND DISCUSSION

3.1. Characterizing Nanofiltration Membranes for Selective Aluminum Retention. We characterize the membranes using transmission electron microscopy (TEM) and Fourier transform infrared spectroscopy (FTIR), complemented by water flux separation and membrane aging experiments, following the methodology outlined in our prior publication.[23] We employ TEM to provide a high-resolution visualization of the cross-section of the coated membrane (see Figure 2A, reprinted with permission from our prior publication).[23] The TEM analysis, which was conducted after active layer curing and stabilization, confirms that the coated membrane exhibits thin and dense polyelectrolyte and polyamide layers atop a polysulfone support. A magnified view in Figure 2A shows that the thickness of the polyamide and polyelectrolyte layers ranges from 30 to 40 nm and from 35 to 50 nm, respectively, confirming the successful deposition of both selective polymer layers. Our prior publication also presents conducted streaming ζ potential measurements for conventional uncoated and coated membranes. We observe the isoelectric point of the uncoated membrane at pH ~ 5.5, while the coated membrane remains positive between pH 2 and 8.[23] Additionally, our previous work also included a wettability analysis for the uncoated and coated membranes, with advancing contact angle measurements revealing that the polyelectrolyte addition preserves the membrane's apparent hydrophilicity at a 34° contact angle. However, the slower decline rate in contact angle for the coated membrane suggests

https://doi.org/10.1021/acssuschemeng.4c07268
ACS Sustainable Chem. Eng. 2025, 13, 846−858

reduced surface permeability, aligning with water permeability experiment results.[23]

Figure 2B illustrates the Na/Al separation factor of both coated and uncoated membranes, evaluated using sulfate-rich waste cryolite at pH 3. We selected pH 3 for the Na/Al selectivity test, aiming to exemplify the smallest difference in the Na/Al separation factor based on pH profiles previously established for this membrane.[23] As the water flux increases from 14 to 38 LMH, we observe that the Na/Al separation factors for both membranes increase monotonically, from 3.0 to 5.8 for the uncoated membrane and from 6.5 to 9.0 for the coated membrane. On average, at pH 3, the uncoated and coated membranes exhibit a rejection rate of 4.3% and 7.1%, respectively, for the dissolved Na^+. The Al^{3+} rejection for both types of membranes consistently falls within 99.0 ± 0.1%. Samples of the pH 3 sulfate solutions at four different transmembrane fluxes show that, on average, the permeation rate of Na^+ is 65.1% greater with the coated membrane than the uncoated membrane, effectively separating it from the retained Al^{3+}. Consequently, the coated membrane consistently exhibits a separation factor approximately 100−200% higher than that of the uncoated membrane across the tested water flux range. Our experimental results indicate that nanofiltration membranes with a higher density of positively charged groups at the membrane−solution interface lead to greater selectivity for monovalent cations. This observation is in line with previous studies on enhanced Donnan exclusion NF membranes.[23,28,32] Due to its increased selectivity, we focus the subsequent experimental optimization of process conditions solely on the coated NF membrane.

The FTIR spectrum of the polyamide, polyelectrolyte, and polysulfone layers is shown in Figure 2C for pH values ranging from 2 to 10.[50] Following the protocol developed by Villalobos et al.,[51] we first remove the polyester mesh from both the coated and uncoated membranes, allowing infrared waves to penetrate, and we then collect the absorbance and transmittance data. Here, we chose not to apply chloroform or dimethylformamide to dissolve the polysulfone support, as these solvents may destabilize or depolymerize the polyelectrolyte layer. The FTIR transmission spectrum of the uncoated membrane reveals three key features across all pH values: a broad peak from 3200 to 3600 cm^{-1} corresponding to primary and secondary N−H stretchings in the ammonium group, a sharp bump between 2800 and 2900 cm^{-1} for C−H stretching in the aliphatic structure, and a distinct peak at 1730 cm^{-1} for C═O stretching in the carboxylate group.[50] In comparison, the coated membrane exhibits peaks at the same wavenumbers, with notable differences including a less pronounced peak for C═O stretching and a markedly deeper peak for N−H stretching. The differences in transmittance between the two membranes suggest that the polyelectrolyte coating increases the density of ammonium groups, as indicated by the deeper N−H peak across the spectrum of tested pH values. Together with the ζ potential measurements and TEM images, these measurements reaffirm the successful deposition of the electropositive polyelectrolyte coating on the polyamide NF membrane, enhancing the charge-based exclusion of multivalent cations.

Lastly, we conduct aging tests on the coated membrane to evaluate its acid tolerance, as depicted in Figure 2D. For these tests, we submerge three coated membranes in 0.5 M HCl and measure the species rejections of a pH 1 chloride-rich waste cryolite solution over 4 weeks. Throughout this period, the coated membrane retains its ability to strongly reject Al^{3+} ions and allow the permeation of monovalent ions. We observe that the species rejections fluctuate by less than ∼10%, indicating that the membrane maintains its selectivity performance over extended exposure to acidic conditions. Further, no visible structural changes or active layer delamination were observed during the acid aging experiments. Therefore, this suggests that the coated membrane is capable of sustained operation in acidic waste cryolite environments.

3.2. Calibrating Transport Models using Coupon-Scale Experiments with Waste Cryolite Solutions. In this section, we report coupon-scale experiments with the coated membrane and the sulfate- and chloride-rich waste cryolite solutions, which are conducted with the experimental apparatus as illustrated in Figure 3A.[28] Here, we compile over 200 original ion rejection measurements that are subsequently used to calibrate the DSPM-DE in Figure 3B, to facilitate module- and process-scale analyses.[41] In the experiments, we utilize 8.0 cm by 3.0 cm coupons of coated NF membrane with both sulfate-rich and chloride-rich solutions at pH 1, 2, and 3, to examine the influence of process conditions and the impact of H_2SO_4 and HCl as leaching agents.[18] The experiments are conducted with the coated membrane because of the enhanced Na/Al selectivity provided by the magnified Donnan exclusion effect from the polyelectrolyte surface coating, as discussed in Section 3.1.[23]

Panels C−H of Figure 3 illustrate the ion rejection as a function of driving water flux for the coated NF membrane with chloride- and sulfate-rich waste cryolite solutions, with solution pH ranging from 1 to 3. The solid markers indicate the measured rejection data points, while the curved solid lines represent the model predictions. The calibrated model outputs show strong agreement with the experimental data, registering a mean-square error of less than 5% across the tested conditions.

In all cases, the measured species rejections increase monotonically with water flux.[26,35] Al^{3+} consistently exhibits high rejection rates, with an average of 99.1% and all measurements exceeding 97.6%. With the chloride-rich cryolite solution, the coated NF membrane shows near-complete rejection of Al^{3+}, with an average rejection of 99.4% across all 12 samples. In contrast, monovalent ions display significantly higher permeation rates through the membrane; for example, Na^+, Li^+, and K^+ are rejected at average rates of 26.3%, 12.6%, and 31.5%, respectively. Based on the DSPM-DE model, we attribute this differential permeation to a combination of steric, Donnan, and dielectric exclusion mechanisms, which align with longstanding experimental evidence regarding monovalent selectivity of nanofiltration membranes.[26,34,38,52,53]

Additionally, our experiments find that the coated NF membrane demonstrates significantly lower permeation rates for monovalent ions in sulfate-rich waste cryolite solutions compared with chloride-rich solutions. As shown in Figure 3C−E, the rejection of Na^+ averages 88.8% or 2.4 times higher than the rejection rate observed in chloride-rich cryolite, which stands at 26.3%. This observation aligns with our prior experimental and molecular dynamics studies,[23,28,54] which can be attributed to cation−anion transport coupling across the membrane's active layer, necessitated by the requirement to maintain electroneutrality in permeation rates.[26] Sulfate ions, characterized by their large hydrated radii, high valency, and low diffusivity, show low sorption selectivity into the membrane.[28] Consequently, sulfate ions typically exhibit

https://doi.org/10.1021/acssuschemeng.4c07268
ACS Sustainable Chem. Eng. 2025, 13, 846−858

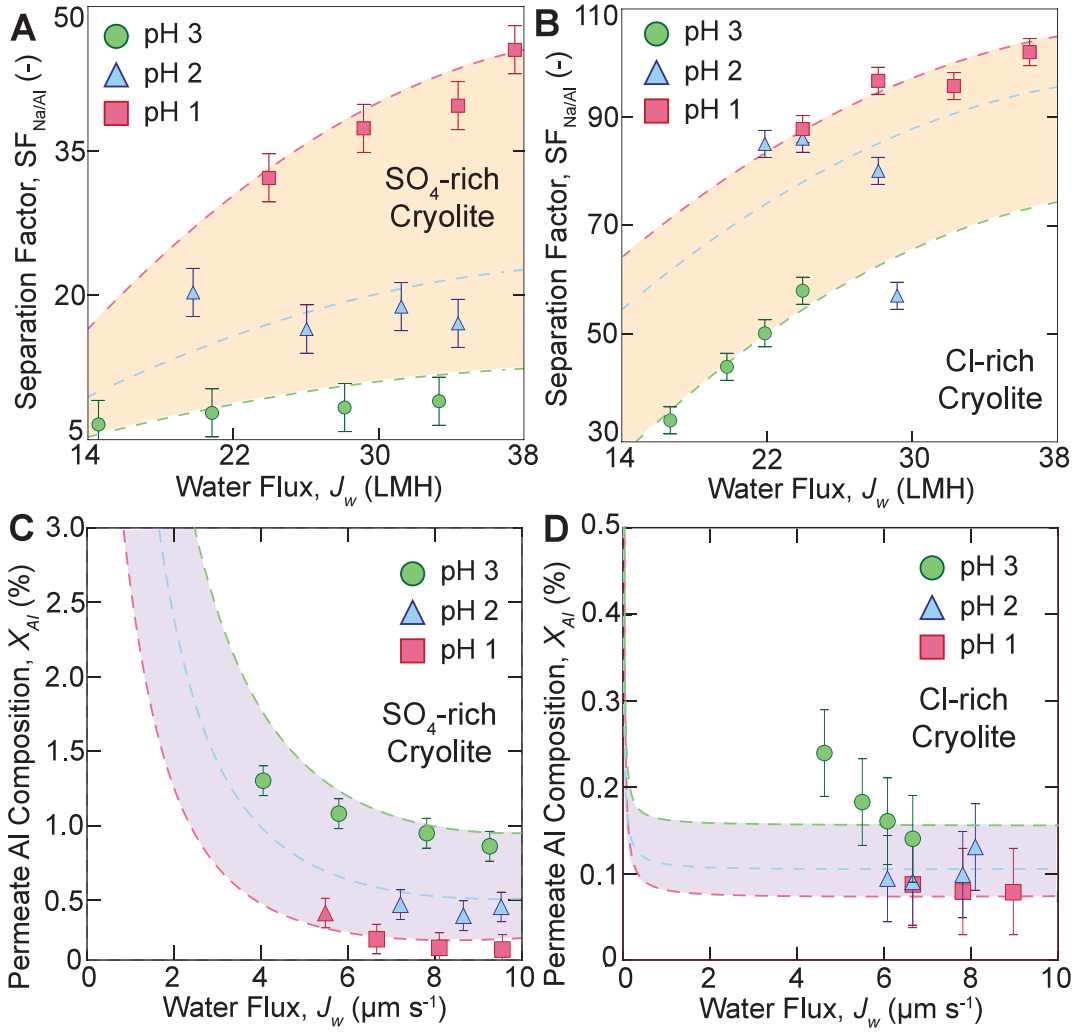

Figure 4. Plot of the Na/Al separation factor for the (A) sulfate-rich cryolite and (B) chloride-rich cryolite solutions at solution pH of 1−3 as a function of the transmembrane flux with the coated NF membrane. Plot of the percentage composition of Al in the permeate stream for the (C) sulfate-rich and (D) chloride-rich cryolites at solution pH values of 1−3, as a function of the transmembrane flux. All four panels demonstrate that permeate streams with higher monovalent cation purity are facilitated by increased transmembrane flux and lower solution pH.

rejection rates exceeding 95%, in contrast to chloride ions, which have rejection rates ranging from 20−50%. The high rejection rates of sulfate ions lead to elevated rejection of monovalent cations, as the membrane system compensates to preserve electroneutrality in the permeate stream.

Furthermore, the membrane's monovalent cation selectivity for both sulfate- and chloride-rich waste cryolites improves as the solution pH decreases. This enhancement in monovalent cation selectivity corresponds to an increase in ζ potential and a higher density of ammonium groups within the active layer.[23] Our experiments show that as the solution pH is reduced from 3 to 1, the permeation rate of Al^{3+} decreases from 1.2% to 0.7% with chloride-rich cryolite and from 0.5% to 0.3% with sulfate-rich cryolite. Conversely, the permeation of Na^+ increases from 68.2% to 70.6% with chloride-rich cryolite and from 4.7% to 14.2% with sulfate-rich cryolite, over the same pH range. Under lower solution pH conditions, the density of positively charged ammonium groups increases due to ionic equilibria, leading to a stronger Donnan exclusion effect that reduces the partitioning of Al^{3+} into the membrane.[55] Meanwhile, SO_4^{2-} and Cl^- experiences increased partitioning.[34] To maintain permeate electroneutrality, our models suggest that additional Na^+, K^+, and Li^+ ions are partitioned and transported across the membrane, resulting in increased apparent permeation rates under lower pH conditions.[28]

3.3. Quantifying the Impacts of Process Conditions on Apparent Monovalent Selectivity. In this section, we analyze the impact of the solution pH, anion composition, and driving water flux on the observed monovalent selectivity of the coated NF membrane. Panels A and B of Figure 4 depict the impact of the solution pH of sulfate-rich and chloride-rich solutions on the Na/Al separation factor, respectively. The solid markers denote coupon-scale experimental measurements, while the dashed lines represent the model outputs from the calibrated DSPM-DE. An NF process with a high $SF_{Na/Al}$ can produce Al^{3+}-depleted permeate streams, potentially allowing for environmentally benign disposal.[18] The $SF_{Na/Al}$ values in sulfate- and chloride-rich cryolite solutions consistently exceed unity across the range of tested pH and water flux conditions, indicating selective permeation of Na^+ over Al^{3+}. Generally, $SF_{Na/Al}$ increases with higher water fluxes and lower solution pH. With pH 1 solutions, notably, sulfate-rich and chloride-rich cryolite solutions attain $SF_{Na/Al}$ values as high as 45.51 and 102.02, respectively.

https://doi.org/10.1021/acssuschemeng.4c07268
ACS Sustainable Chem. Eng. 2025, 13, 846−858

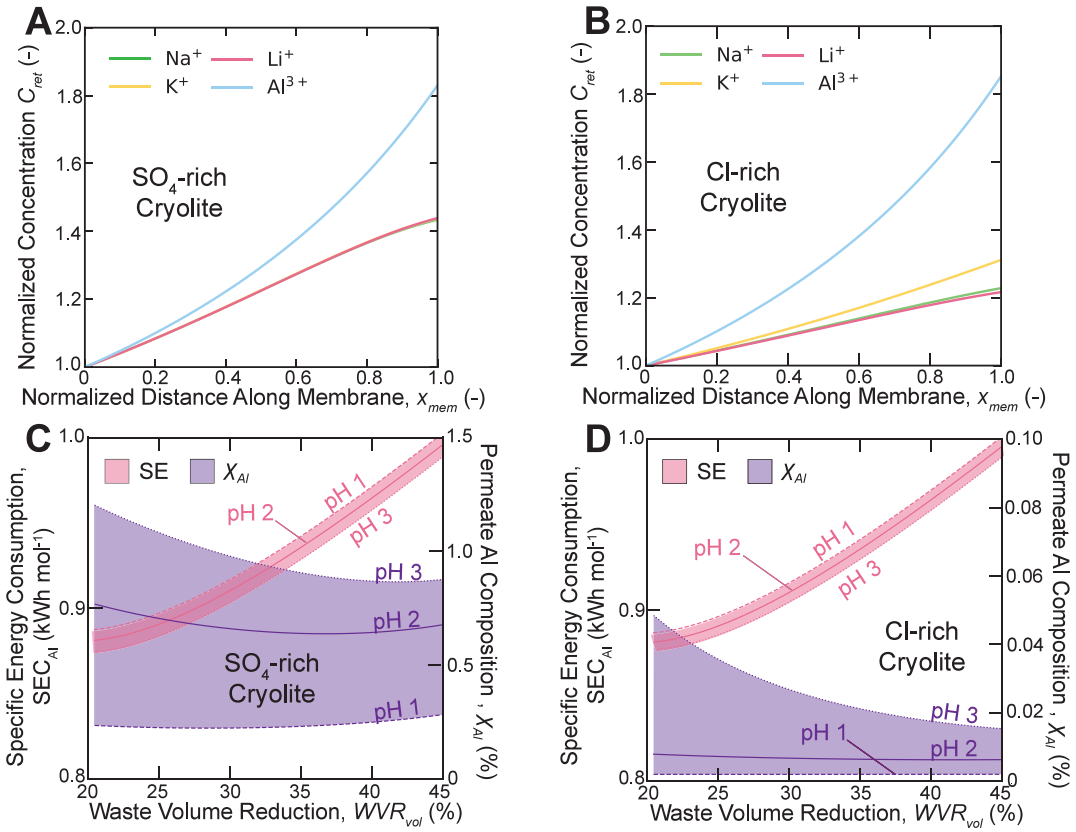

Figure 5. Plot of the normalized ion concentration in the retentate stream as a function of the normalized distance along the membrane length for (A) sulfate and (B) chloride-rich cryolite. The normalized concentrations of the ions increase along the length of the membrane due to selective water extraction by the polyamide membrane. The greater increase in the Al^{3+} concentration indicates selective retention relative to the monovalent cations. Plot of the specific energy consumption and the permeate Al composition as functions of the (C) sulfate and (D) chloride cryolite pH and the waste volume reduction.

Furthermore, we observe that the $SF_{Na/Al}$ is higher with cryolite solutions at lower pH levels. For example, $SF_{Na/Al}$ rises from 9.0 to 45.5 in sulfate-rich cryolite and from 57.9 to 102.0 in chloride-rich cryolite. These findings correlate with the trends in Na^+ and Al^{3+} permeation rates discussed in Section 3.2. Lower pH levels increase the positive charge density of the active layer in the NF membrane due to the protonation of ammonium groups, enhancing the Donnan exclusion effect.[56] This yields decreased partitioning of multivalent cations like Al^{3+} and an improved $SF_{Na/Al}$.[55] Conversely, the lower Na^+ permeation rates observed with sulfate-rich solutions, as discussed in Section 3.2, result in reduced relative permeation rates of Na^+ compared to Al^{3+}, leading to a decreased $SF_{Na/Al}$ due to sulfate anion transport coupling.[28]

Panels C and D of Figure 4 present the effects of solution pH and transmembrane flux on the concentration of Al^{3+} ions in the permeate stream for both sulfate-rich and chloride-rich solutions. A lower percentage of Al^{3+} ions in the permeate indicates that the NF membrane selectively permeates the relatively benign Na^+ and K^+ ions instead of Al^{3+}. This results in a permeate stream that is more suitable for environmentally benign waste disposal, while the retentate stream has a higher aluminum purity.

In general, the permeate aluminum composition (χ_{Al}) decreases with increasing driving water fluxes. For example, with pH 3 sulfate- and chloride-rich cryolite solutions, χ_{Al} decreases from 1.38% to 0.79% and from 0.23% to 0.14%, respectively, across the range of experimental water fluxes. As the solution pH decreases from 3 to 1, the χ_{Al} of the permeate stream further decreases from 0.79% to 0.07% for the sulfate-rich cryolite and from 0.14% to 0.08% for the chloride-rich cryolite. The observed reduction in χ_{Al} with increasing water fluxes and lower solution pH aligns with the previously discussed trends in Na/Al selectivity and the permeation rates of Al^{3+} and Na^+, indicating that the overall improvement in permeate quality is a feasible result of enhanced Donnan exclusion effects.

Our coupon-scale experiments with sulfate- and chloride-rich solutions demonstrate that the coated NF membrane provides enhanced Na/Al separation, likely due to the improved Donnan exclusion of multivalent cations. For cryolite solutions at pH 1, which is similar to the acidity of acid leachates from bauxite processing,[18] the aluminum content in the permeate can be reduced to as little as 0.07% and 0.08% for sulfate- and chloride-rich cryolites, respectively. This suggests that variations in anionic composition and the acid-leaching process have a minimal impact on the purity of the resulting permeate. Additionally, the low aluminum concentration in the permeate suggests that the Na- and K-rich permeate is more sufficiently pure for environmentally safe disposal via post-treatment measures. The aluminum concentration is reduced by 2 orders of magnitude from the feed to the permeate, from 4.41 g L^{-1} to as low as 0.0138 g L^{-1}. Our data suggest that this solution of low aluminum concentration can be further treated with a membrane or ion-exchange step before environmentally benign disposal.[57,58] Further, the total dissolved solids (TDS)

https://doi.org/10.1021/acssuschemeng.4c07268
ACS Sustainable Chem. Eng. 2025, 13, 846−858

in the permeate, reaching as low 1.17 g L^{-1}, and concentration of aluminum, fall within a general threshold for industrial effluent of 1.5 g L^{-1} and 0.1 g L^{-1}, respectively.[59,60]

Meanwhile, aluminum is effectively retained in the retentate stream. A sufficiently aluminum-pure retentate stream can partially replace the electrolyte in the Hall−Héroult process. Regularly removing a portion of the spent cryolite electrolyte and replacing it with fresh, higher-purity cryolite help dilute the impurities and maintain a more consistent quality of the electrolyte over time. In more extreme cases, it may be necessary to fully replace the bath with a high-purity cryolite electrolyte.[18] Regardless, the retentate stream provides an opportunity to recycle waste cryolite back into the molten salt electrolysis process. An appropriately sized NF module could concentrate aluminum for successful recirculation and further aluminum production, as we will explore with module-scale analysis in the next section.

3.4. Projecting Module-Scale Performance of Nanofiltration for Aluminum Recycling from Waste Cryolite. Finally, we conduct module-scale simulations to evaluate the feasibility of Donnan-enhanced nanofiltration for recovering a high-purity aluminum stream and an Al-depleted stream that is considerably safer for disposal. As detailed in Section 2.2.2, we modeled the process using a commercial-scale spiral-wound membrane module (Nitto-Denko PRO XS1) equipped with the same coated NF membrane. Through this analysis, we quantify the concentration ratio of Na/Al in the permeate and retentate streams and assess the potential effectiveness of a membrane unit in achieving resource circularity in aluminum production. The nodal ion fluxes are calculated using the calibrated DSPM-DE model and integrated with a forward Euler scheme to determine the net composition and flow rates of the permeate and retentate streams. We also calculate the projected specific energy consumption as a function of waste volume reduction and the expected aluminum composition in the permeate from a spiral-wound module. The isentropic efficiencies of the high-pressure pump and energy recovery device are assumed to be 0.75 and 0.80, respectively.[49]

Panels A and B of Figure 5 show the normalized ion concentrations in the retentate stream along the membrane length for sulfate- and chloride-rich waste cryolite solutions, respectively. The results indicate that the concentrations of Na^+, Li^+, K^+, and Al^{3+} in the retentate stream increase along the membrane length due to selective water extraction by the membrane. Additionally, with both solution compositions, the retentate solution exhibits a notably higher increase in Al^{3+} concentrations compared to that of the other monovalent ions. These results suggest that monovalent ions permeate through the NF membrane much faster than Al^{3+}, which is consistent with the coupon-scale experimental results presented in Sections 3.2 and 3.3. With the sulfate-rich cryolite solution, the concentrations of Na^+, Li^+, and K^+ increase from 1 to approximately 1.42 along the length of the module. In contrast, with the chloride-rich cryolite, these ions increase from 1 to around 1.2. As discussed in Sections 3.2 and 3.3, this difference in the relative concentration in the retentate stream results from the anion−cation coupling between sulfate and the monovalent cations; the low permeability of sulfate ions leads to reduced net permeation of the monovalent cations due to the electroneutrality condition in the permeate stream, resulting in a higher concentration rate with the sulfate-rich cryolite. Nevertheless, across both solution compositions, the enhanced Donnan exclusion afforded by the membrane's positively charged surface contributes to the superior rejection of multivalent Al^{3+}, thus leading to its selective retention.

Next, we analyze the Na/Al concentration ratio in the retentate stream as a function of the waste volume reduction (WVR) ratio, commonly referred to as the recovery ratio in desalination literature.[61] As previously stated, the Na/Al ratio is important to ensure efficient aluminum production. The recovery ratio, defined as the ratio of permeate volume to feed volume, represents the percentage of non-aluminum-containing solution recovered from the feed. Under optimal conditions, the permeate contains primarily monovalent ions requiring disposal or further treatment; on the other hand, the aluminum-rich retentate is suitable for reblending with bauxite input, promoting a circular economy in aluminum production. Our results show that the retentate Na/Al ratio generally increases with decreasing solution pH for both waste cryolite compositions due to enhanced Na/Al separation factors. For example, at a 25% waste volume reduction, when the pH drops from 3 to 1, the Na/Al ratio decreases from 4.06 to 3.95 in sulfate-rich cryolite and from 3.38 to 3.35 in chloride-rich cryolite. As the WVR ratio increases, more Na^+, Li^+, and K^+ are removed into the permeate stream, further lowering the Na/Al ratio in the retentate. For instance, at pH 1, the Na/Al ratio decreases from 3.35 to 2.73 in chloride-rich cryolite as the WVR increases from 25% to 45%. For recycling purposes, the aluminum-rich retentate should ideally have a Na/Al concentration ratio around 2.5.[18] Under the experiments' most optimistic tested parameters, a single nanofiltration stage can achieve a retentate Na/Al ratio of approximately 2.6, while reducing the volume of waste cryolite requiring further treatment by up to 45%, highlighting significant potential for resource recovery and waste minimization.

Panels C and D of Figure 5 show the specific energy consumption (SEC) as a function of solution pH and waste volume reduction, also known as the recovery ratio. Here, we report SEC in kWh per mol to more accurately reflect the energy required to recover each mole of aluminum. Generally, higher waste volume reduction leads to increased specific energy consumption, as greater hydraulic pressures are required to overcome the higher osmotic pressure necessary for greater permeate recovery, consistent with prior membrane studies.[62] For example, the SEC increases from 0.896 kWh mol^{-1} to 1.002 kWh mol^{-1} as the WVR rises from 25% to 45% for chloride-rich cryolite at pH 1. Additionally, lower pH treatments require more energy for both solution compositions due to lower ionic permeability, as discussed in Sections 3.2 and 3.3. Specifically, at a 45% recovery ratio, energy consumption rises from 0.989 kWh mol^{-1} to 1.002 kWh mol^{-1} for sulfate-rich cryolite and from 0.990 kWh mol^{-1} to 1.002 kWh mol^{-1} for chloride-rich solutions as the solution pH decreases from 3 to 1. This finding aligns with previous bench-scale experiments, which demonstrate that lower pH levels enhance the Donnan exclusion effect by increasing the density of positively charged NH_2^+ groups on the polyelectrolyte layer. As such, this enhancement makes the membrane more resistant to cationic transport and raises energy requirements.[23,28]

Panels C and D of Figure 5 also illustrate the permeate aluminum composition after one NF treatment stage with sulfate- and chloride-rich cryolite, respectively. Generally, lower pH solutions result in a purer permeate stream of monovalent cations due to the higher Na/Al selectivity, as evidenced by a decrease in aluminum composition. Moreover,

https://doi.org/10.1021/acssuschemeng.4c07268
ACS Sustainable Chem. Eng. 2025, 13, 846−858

chloride-rich cryolite produces a significantly purer permeate stream than sulfate-rich cryolite. For example, at pH 1 and a 45% recovery ratio, the chloride solution contains 0.00194% Al, compared to 0.285% in the sulfate solution. This outcome is consistent with the differences in separation factors discussed in Section 3.3, which result from the lower Na^+ levels induced by sulfate−cation coupling to maintain permeate electroneutrality in sulfate-rich cryolite solutions. Still, the extremely low Al^{3+} concentrations in the permeate streams for both sulfate- and chloride-rich cryolites indicate that NF is highly effective in extracting Na^+-rich permeate.

In conclusion, the module-scale analysis using the experimentally validated DSPM-DE and a commercial spiral-wound NF system shows the effective treatment of waste cryolite. This process results in an Al^{3+}-depleted permeate, with aluminum concentrations as low as 0.00194%, possibly suitable for environmentally safe disposal. Further, the retentate stream achieves a Na/Al concentration ratio of approximately 2.6, making it viable for recycling in cryolite−alumina molten salt electrolysis. The analysis indicates that lower pH levels and higher recovery ratios enhance the Na/Al separation, reducing the aluminum content in the permeate. These findings suggest that Donnan-enhanced nanofiltration can significantly contribute to resource recovery and waste minimization in the aluminum industry with further optimizations potentially improving system efficiency and sustainability.

4. SUMMARY AND IMPLICATIONS FOR RESOURCE CIRCULARITY

In this study, we explored the performance of two nanofiltration (NF) membranes—one uncoated and the other coated with a polyelectrolyte layer—for their ability to selectively separate aluminum from waste cryolite solutions. Utilizing characterization techniques, such as TEM and FTIR, we examined the structural attributes and functional improvements imparted by the polyelectrolyte coating. This coating significantly enhances the density of positively charged ammonium groups on the membrane surface, thereby bolstering the membrane's capability to exclude multivalent cations like Al^{3+} and improving the Na/Al separation factor. Our experimental findings reveal that the coated membrane significantly outperforms its uncoated counterpart, with Na/Al separation factors that rise from 6.5 to 9.0 as water flux increases, compared to a range of 3.0−5.8 for the uncoated membrane. The superior selectivity for monovalent cations demonstrated by the coated membrane can be attributed to the enhanced Donnan exclusion effect.

Through coupon-scale experiments, we demonstrated the coated NF membrane's ability to maintain high rejection rates for Al^{3+}, averaging 99.1% across all test conditions, while allowing substantial permeation of Na^+, Li^+, and K^+. This selective permeability is particularly pronounced at lower pH levels, where the Donnan exclusion effect is amplified due to an increased density of positive charges on the membrane surface. Specifically, we observed that lower pH solutions significantly enhance the Na/Al separation factor, with the coated membrane achieving high selectivity, reaching 102.02 in chloride-rich cryolite solutions. This enhanced selectivity, along with reduced aluminum content in the permeate, underscores the membrane's capability to produce Na- and K-rich streams that meet general industrial effluent thresholds and, therefore, are potentially environmentally safe for disposal with post-treatment steps.

Our module-scale simulations, conducted by using the DSPM-DE model, further validated the practical viability of Donnan-enhanced nanofiltration for processing waste cryolite. These simulations demonstrated the process's efficiency in concentrating Al^{3+} in the retentate while producing an Al-depleted permeate, with aluminum concentrations as low as 0.00194%. The retentate stream, achieving a Na/Al concentration ratio of approximately 2.6, is likely suitable for recycling in aluminum processing. We found that both lower pH levels and higher recovery ratios augment Na/Al separation, thus lowering the aluminum content in the permeate. These outcomes are consistent with our experimental data, emphasizing the DSPM-DE model's robustness in predicting membrane performance under varying conditions.

In conclusion, our study demonstrates the potential effectiveness of nanofiltration membranes in selectively retaining aluminum from waste cryolite solutions, thereby promoting resource recovery and minimizing waste during the aluminum refinery. The Donnan-enhanced nanofiltration process not only generates high-purity aluminum streams suitable for recycling but also produces an Al-depleted permeate that progresses significantly toward a safe disposable effluent.

While our results are promising for hypersaline cryolite waste treatment, we recognize that cryolite waste compositions differ widely across aluminum refineries. Further testing with local waste compositions is essential to optimize the membrane's properties and operating conditions, tailoring the process for specific plant requirements. This customization is crucial for achieving a commercially viable and scalable membrane process that can handle the distinct osmotic and chemical characteristics inherent to varied industrial waste streams. Additional research could aim to further refine membrane properties and optimize operational conditions to enhance system efficiency and sustainability, broadening the scope of this technology's application in industrial aluminum processing and waste management.

■ ASSOCIATED CONTENT

Supporting Information

The Supporting Information is available free of charge at https://pubs.acs.org/doi/10.1021/acssuschemeng.4c07268.

Further details on the bench-scale experimental apparatus; derivation of retentate concentration calculation in eq 22; original experimental data for 200 nanofiltration ion concentration measurements with waste aluminum cryolite solutions (PDF)

■ AUTHOR INFORMATION

Corresponding Author

John H. Lienhard − *Department of Mechanical Engineering, Massachusetts Institute of Technology, Cambridge, Massachusetts 02139, United States;* orcid.org/0000-0002-2901-0638; Email: lienhard@mit.edu

Authors

Trent R. Lee − *Department of Mechanical Engineering, Massachusetts Institute of Technology, Cambridge, Massachusetts 02139, United States*

Zi Hao Foo − *Department of Mechanical Engineering and Center for Computational Science and Engineering, Massachusetts Institute of Technology, Cambridge, Massachusetts 02139, United States;* orcid.org/0000-0002-7474-7065

Vinn Nguyen − *Department of Mechanical Engineering, Massachusetts Institute of Technology, Cambridge, Massachusetts 02139, United States*

Complete contact information is available at: https://pubs.acs.org/10.1021/acssuschemeng.4c07268

Author Contributions

T.R.L. conducted the experiments and the coupon-scale analysis. Z.H.F. conducted the module-scale analysis. V.N. assisted with the coupon-scale analysis. J.H.L. supervised the project. The manuscript was prepared and reviewed by all of the authors.

Notes

The authors declare no competing financial interest.

■ ACKNOWLEDGMENTS

T.R.L. acknowledges funding support from the MIT Energy Initiative. Z.H.F. acknowledges funding support from the MathWorks Fellowship and the NUS Development Grant. Any opinions, findings, and conclusions or recommendations expressed in this material are those of the author(s) and do not necessarily reflect the views of their respective funding agencies.

■ REFERENCES

(1) Gautam, M.; Pandey, B.; Agrawal, M. In *Environmental Carbon Footprints*; Muthu, S. S., Ed.; Butterworth-Heinemann, 2018; pp 197−228. DOI: 10.1016/B978-0-12-812849-7.00008-8.

(2) Brough, D.; Jouhara, H. The aluminium industry: A review on state-of-the-art technologies, environmental impacts and possibilities for waste heat recovery. *International Journal of Thermofluids* **2020**, *1*−*2*, 100007.

(3) Wu, S.; Tao, W.; Han, W.; Ge, H.; Chen, L.; Yang, J.; Zheng, Y.; He, J.; Yang, Y.; Wang, Z. Hydrometallurgical stepwise separation of alumina and recovery of aluminum fluoride from waste anode cover material of aluminum electrolysis. *Minerals Engineering* **2022**, *186*, 107740.

(4) Langhorst, M.; Billy, R. G.; Schwotzer, C.; Kaiser, F.; Müller, D. B. Inertia of Technology Stocks: A Technology-Explicit Model for the Transition toward a Low-Carbon Global Aluminum Cycle. *Environ. Sci. Technol.* **2024**, *58*, 9624−9635.

(5) Blaesing, L.; Walnsch, A.; Hippmann, S.; Modrzynski, C.; Weidlich, C.; Pavón, S.; Bertau, M. Ferrosilicon Production from Silicon Wafer Breakage and Red Mud. *ACS Sustainable Resource Management* **2024**, *1*, 404−416.

(6) Pereira, L. C.; Corrêa, C. R.; Zilnyk, K. D.; Hias, E. O.; Santos, H. C.; Yamamoto, H.; Barros, J. L.; Yamaji, F. M. Binchotan Charcoal as an Alternative to Calcined Petroleum Coke in Anodes in the Aluminum Industry. *ACS Sustainable Chem. Eng.* **2024**, *12*, 11480−11487.

(7) Coke, L. B.; Weir, C. C.; Hill, V. G. Environmental Impact of Bauxite Mining and Processing in Jamaica. *Social and Economic Studies*; Sir Arthur Lewis Institute of Social and Economic Studies, 1987; Vol. *36*, pp 289−333.

(8) Pradhan, G.; Tripathy, B.; Ram, D. K.; Digal, A. K.; Das, A. P. Bauxite Mining Waste Pollution and Its Sustainable Management through Bioremediation. *Geomicrobiology Journal* **2024**, *41*, 335−344.

(9) Khairul, M. A.; Zanganeh, J.; Moghtaderi, B. The composition, recycling and utilisation of Bayer red mud. *Resources, Conservation and Recycling* **2019**, *141*, 483−498.

(10) S. R, R.; R., R.; B, N. Sustainable Management of Red Mud: Life Cycle Assessment and Treatment Techniques. *Int. J. Multidiscip. Res.* **2024**, *6*, IJFMR240112525.

(11) Ky, L.; Ly, H.; Kh, T.; Yy, T.; Sp, L.; Am, Q.; T, P.; R, N. Environmental and Occupational Health Impact of Bauxite Mining in Malaysia: A Review. *Int. Med. J. Malays.* **2017**, *16*, 137−150.

(12) Dey, S.; Tripathy, B.; Kumar, M. S.; Das, A. P. Ecotoxicological consequences of manganese mining pollutants and their biological remediation. *Environmental Chemistry and Ecotoxicology* **2023**, *5*, 55−61.

(13) Kamble, P. H. Environmental Impact of Bauxite Mining: A Review. *International Journal for Research in Applied Science and Engineering Technology* **2019**, *7*, 86−90.

(14) Lemougna, P. N.; Wang, K.-t.; Tang, Q.; Cui, X.-m. Synthesis and characterization of low temperature (<800 °C) ceramics from red mud geopolymer precursor. *Construction and Building Materials* **2017**, *131*, 564−573.

(15) Silveira, N. C. G.; Martins, M. L. F.; Bezerra, A. C. S.; Araújo, F. G. S. Red Mud from the Aluminium Industry: Production, Characteristics, and Alternative Applications in Construction Materials—A Review. *Sustainability* **2021**, *13*, 12741.

(16) Ishak, R.; Laroche, G.; Lamonier, J.-F.; Ziegler, D. P.; Alamdari, H. Characterization of Carbon Anode Protected by Low Boron Level: An Attempt To Understand Carbon−Boron Inhibitor Mechanism. *ACS Sustainable Chem. Eng.* **2017**, *5*, 6700−6706.

(17) Kvande, H.; Drablos, P. A. The Aluminum Smelting Process and Innovative Alternative Technologies. *J. Occup. Environ. Med.* **2014**, *56*, S23−S32.

(18) Tang, C.; Wang, J.; Yang, S.; Zhang, X.; Li, S.; Lai, Y.; Tian, Z.; Jin, S.; Chen, Y. Efficient extraction and recovery of lithium from waste aluminum cryolite electrolyte. *Resources, Conservation & Recycling* **2023**, *197*, 107070.

(19) Li, X.; Liu, Y.; Zhang, T.-a. A comprehensive review of aluminium electrolysis and the waste generated by it. *Waste Management & Research* **2023**, *41*, 1498−1511.

(20) Cao, X.; Peng, J.; Dong, W.; Li, Y.; Wang, Y.; Di, Y. Review on the Preparation of Cryolite from Industry Waste Containing Fluorine. *Journal of Sustainable Metallurgy* **2024**, *10*, 419−434.

(21) Tao, W.; Yang, J.; Chen, L.; Zhang, Y.; Wu, S.; Li, J.; Liu, Z.; He, J.; Wang, Z. Sustainable Recovery of Fluorine from Waste Aluminum Electrolyte by Sulfuric Acid Baking. *Journal of Sustainable Metallurgy* **2023**, *9*, 1201−1214.

(22) Wu, S.; Tao, W.; Ge, H.; Yang, J.; Chen, L.; He, J.; Yang, Y.; Wang, Z. Extraction and recycling of fluoride-containing phase from spent bottom sedimentation of aluminum smelting cell by leaching in Al3+ solution media. *Sep. Purif. Technol.* **2023**, *306*, 122797.

(23) Foo, Z. H.; Liu, S.; Kanias, L.; Lee, T. R.; Heath, S. M.; Tomi, Y.; Miyabe, T.; Keten, S.; Lueptow, R. M.; Lienhard, J. H. Positively-Coated Nanofiltration Membranes for Lithium Recovery from Battery Leachates and Salt-Lakes: Ion Transport Fundamentals and Module Performance. *Adv. Funct. Mater.* **2024**, *34*, 2408685.

(24) Zhao, Y.; Tong, X.; Chen, Y. Fit-for-Purpose Design of Nanofiltration Membranes for Simultaneous Nutrient Recovery and Micropollutant Removal. *Environ. Sci. Technol.* **2021**, *55*, 3352−3361.

(25) Lin, J.; Ye, W.; Huang, J.; Ricard, B.; Baltaru, M.-C.; Greydanus, B.; Balta, S.; Shen, J.; Vlad, M.; Sotto, A.; Luis, P.; Van Der Bruggen, B. Toward Resource Recovery from Textile Wastewater: Dye Extraction, Water and Base/Acid Regeneration Using a Hybrid NF-BMED Process. *ACS Sustainable Chem. Eng.* **2015**, *3*, 1993−2001.

(26) Wang, R.; Lin, S. Pore model for nanofiltration: History, theoretical framework, key predictions, limitations, and prospects. *J. Membr. Sci.* **2021**, *620*, 118809.

(27) Guo, S.; Wan, Y.; Chen, X.; Luo, J. Loose nanofiltration membrane custom-tailored for resource recovery. *Chem. Eng. J.* **2021**, *409*, 127376.

(28) Foo, Z. H.; Rehman, D.; Bouma, A. T.; Monsalvo, S.; Lienhard, J. H. Lithium Concentration from Salt-Lake Brine by Donnan-Enhanced Nanofiltration. *Environ. Sci. Technol.* **2023**, *57*, 6320−6330.

(29) Chung, H. W.; Nayar, K. G.; Swaminathan, J.; Chehayeb, K. M.; Lienhard, J. H. Thermodynamic analysis of brine management methods: Zero-discharge desalination and salinity-gradient power production. *Desalination* **2017**, *404*, 291−303.
(30) Cheng, C.; Yaroshchuk, A.; Bruening, M. L. Fundamentals of selective ion transport through multilayer polyelectrolyte membranes. *Langmuir* **2013**, *29*, 1885−1892.
(31) Wang, R.; Alghanayem, R.; Lin, S. Multipass Nanofiltration for Lithium Separation with High Selectivity and Recovery. *Environ. Sci. Technol.* **2023**, *57*, 14464−14471.
(32) Wang, L.; Rehman, D.; Sun, P. F.; Deshmukh, A.; Zhang, L.; Han, Q.; Yang, Z.; Wang, Z.; Park, H. D.; Lienhard, J. H.; Tang, C. Y. Novel Positively Charged Metal-Coordinated Nanofiltration Membrane for Lithium Recovery. *ACS Appl. Mater. Interfaces* **2021**, *13*, 16906−16915.
(33) Wang, R.; He, R.; He, T.; Elimelech, M.; Lin, S. Performance metrics for nanofiltration-based selective separation for resource extraction and recovery. *Nature Water* **2023**, *1*, 291−300.
(34) Yaroshchuk, A.; Bruening, M. L.; Zholkovskiy, E. Modelling nanofiltration of electrolyte solutions. *Adv. Colloid Interface Sci.* **2019**, *268*, 39−63.
(35) Labban, O.; Liu, C.; Chong, T. H.; Lienhard, J. H. Fundamentals of low-pressure nanofiltration: Membrane characterization, modeling, and understanding the multi-ionic interactions in water softening. *J. Membr. Sci.* **2017**, *521*, 18−32.
(36) Foo, Z. H.; Rehman, D.; Coombs, O. Z.; Deshmukh, A.; Lienhard, J. H. Multicomponent Fickian solution-diffusion model for osmotic transport through membranes. *J. Membr. Sci.* **2021**, *640*, 119819.
(37) Wijmans, J. G.; Baker, R. W. The solution-diffusion model: a review. *J. Membr. Sci.* **1995**, *107*, 1−21.
(38) Bowen, W. R.; Mohammad, A. W.; Hilal, N. Characterisation of nanofiltration membranes for predictive purposes — use of salts, uncharged solutes and atomic force microscopy. *J. Membr. Sci.* **1997**, *126*, 91−105.
(39) Aydogan Gokturk, P.; Sujanani, R.; Qian, J.; Wang, Y.; Katz, L. E.; Freeman, B. D.; Crumlin, E. J. The Donnan potential revealed. *Nature. Communications* **2022**, *13*, 5880.
(40) Epsztein, R.; Shaulsky, E.; Dizge, N.; Warsinger, D. M.; Elimelech, M. Role of Ionic Charge Density in Donnan Exclusion of Monovalent Anions by Nanofiltration. *Environ. Sci. Technol.* **2018**, *52*, 4108−4116.
(41) Geraldes, V.; Brites Alves, A. M. Computer program for simulation of mass transport in nanofiltration membranes. *J. Membr. Sci.* **2008**, *321*, 172−182.
(42) Fan, H.; Yip, N. Y. Elucidating conductivity-permselectivity tradeoffs in electrodialysis and reverse electrodialysis by structure-property analysis of ion-exchange membranes. *J. Membr. Sci.* **2019**, *573*, 668−681.
(43) Lu, C.; Hu, C.; Chen, Z.; Wang, P.; Feng, F.; He, G.; Wang, F.; Zhang, Y.; Liu, J. Z.; Zhang, X.; Qu, J. Dehydration-enhanced ion-pore interactions dominate anion transport and selectivity in nanochannels. *Science. Advances* **2023**, *9*, No. eadf841.
(44) Malmir, H.; Epsztein, R.; Elimelech, M.; Haji-Akbari, A. Induced Charge Anisotropy: A Hidden Variable Affecting Ion Transport through Membranes. *Matter* **2020**, *2*, 735−750.
(45) Duignan, T. T.; Zhao, X. S. The Born model can accurately describe electrostatic ion solvation. *Phys. Chem. Chem. Phys.* **2020**, *22*, 25126−25135.
(46) Tow, E. W.; Lienhard, J. H. Quantifying osmotic membrane fouling to enable comparisons across diverse processes. *J. Membr. Sci.* **2016**, *511*, 92−107.
(47) Roy, Y.; Sharqawy, M. H.; Lienhard, J. H. Modeling of flat-sheet and spiral-wound nanofiltration configurations and its application in seawater nanofiltration. *J. Membr. Sci.* **2015**, *493*, 360−372.
(48) Foo, Z. H.; Thomas, J. B.; Heath, S. M.; Garcia, J. A.; Lienhard, J. H. Sustainable Lithium Recovery from Hypersaline Salt-Lakes by Selective Electrodialysis: Transport and Thermodynamics. *Environ. Sci. Technol.* **2023**, *57*, 14747−14759.
(49) Ahdab, Y. D.; Schücking, G.; Rehman, D.; Lienhard, J. H. Cost effectiveness of conventionally and solar powered monovalent selective electrodialysis for seawater desalination in greenhouses. *Applied Energy* **2021**, *301*, 117425.
(50) Tang, C. Y.; Kwon, Y.-N.; Leckie, J. O. Probing the nano-and micro-scales of reverse osmosis membranes-A comprehensive characterization of physiochemical properties of uncoated and coated membranes by XPS, TEM, ATR-FTIR, and streaming potential measurements. *J. Membr. Sci.* **2007**, *287*, 146−156.
(51) Villalobos, L. F.; Pataroque, K. E.; Pan, W.; Cao, T.; Kaneda, M.; Violet, C.; Ritt, C. L.; Hoek, E. M. V.; Elimelech, M. Orientation matters: Measuring the correct surface of polyamide membranes with quartz crystal microbalance. *Journal of Membrane Science Letters* **2023**, *3*, 100048.
(52) Yaroshchuk, A.; Bruening, M. L.; Licón Bernal, E. E. Solution-Diffusion-Electro-Migration model and its uses for analysis of nanofiltration, pressure-retarded osmosis and forward osmosis in multi-ionic solutions. *J. Membr. Sci.* **2013**, *447*, 463−476.
(53) Hilal, N.; Al-Zoubi, H.; Mohammad, A. W.; Darwish, N. A. Nanofiltration of highly concentrated salt solutions up to seawater salinity. *Desalination* **2005**, *184*, 315−326.
(54) Liu, H.; She, Q. Influence of membrane structure-dependent water transport on conductivity-permselectivity trade-off and salt/water selectivity in electrodialysis: Implications for osmotic electrodialysis using porous ion exchange membranes. *J. Membr. Sci.* **2022**, *650*, 120398.
(55) Ritt, C. L.; Werber, J. R.; Wang, M.; Yang, Z.; Zhao, Y.; Kulik, H. J.; Elimelech, M. Ionization behavior of nanoporous polyamide membranes. *Proc. Natl. Acad. Sci. U.S.A.* **2020**, *117*, 30191−30200.
(56) Liu, S.; Ganti-Agrawal, S.; Keten, S.; Lueptow, R. M. Molecular insights into charged nanofiltration membranes: Structure, water transport, and water diffusion. *J. Membr. Sci.* **2022**, *644*, 120057.
(57) Finnerty, C. T.; Childress, A. E.; Hardy, K. M.; Hoek, E. M.; Mauter, M. S.; Plumlee, M. H.; Rose, J. B.; Sobsey, M. D.; Westerhoff, P.; Alvarez, P. J.; Elimelech, M. The Future of Municipal Wastewater Reuse Concentrate Management: Drivers, Challenges, and Opportunities. *Environ. Sci. Technol.* **2024**, *58*, 3−16.
(58) Giwa, A.; Dufour, V.; Al Marzooqi, F.; Al Kaabi, M.; Hasan, S. W. Brine management methods: Recent innovations and current status. *Desalination* **2017**, *407*, 1−23.
(59) Arana Juve, J.-M.; Christensen, F. M. S.; Wang, Y.; Wei, Z. Electrodialysis for metal removal and recovery: A review. *Chemical Engineering Journal* **2022**, *435*, 134857.
(60) Peng, J.; Kumar, K.; Gross, M.; Kunetz, T.; Wen, Z. Removal of total dissolved solids from wastewater using a revolving algal biofilm reactor. *Water Environment Research* **2020**, *92*, 766−778.
(61) Qasim, M.; Badrelzaman, M.; Darwish, N. N.; Darwish, N. A.; Hilal, N. Reverse osmosis desalination: A state-of-the-art review. *Desalination* **2019**, *459*, 59−104.
(62) Warsinger, D. M.; Chakraborty, S.; Tow, E. W.; Plumlee, M. H.; Bellona, C.; Loutatidou, S.; Karimi, L.; Mikelonis, A. M.; Achilli, A.; Ghassemi, A.; Padhye, L. P.; Snyder, S. A.; Curcio, S.; Vecitis, C. D.; Arafat, H. A.; Lienhard, J. H. A review of polymeric membranes and processes for potable water reuse. *Prog. Polym. Sci.* **2018**, *81*, 209−237.

https://doi.org/10.1021/acssuschemeng.4c07268
ACS Sustainable Chem. Eng. 2025, 13, 846−858